RSC Advances

ROYAL SOCIETY OF CHEMISTRY

www.rsc.org/advances

Table of contents graphic:

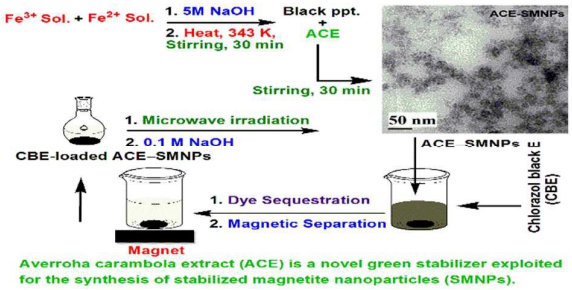

Novel *Averrhoa carambola* extract stabilized magnetite nanoparticles: A green synthesis route for the removal of chlorazol black E from wastewater

Md. Juned K. Ahmed, M. Ahmaruzzaman* and Mushtaq H. Bordoloi

Herein, *Averrhoa carambola* extract (ACE) is exploited as a novel green-stabilizer in the synthesis of stabilized magnetite nanoparticles (SMNPs) for the removal of chlorazol black E. Bare magnetite nanoparticles (BMNPs) were synthesized as reference material and the nanoparticles were characterized with FTIR, XRD, TEM, SAED, EDX, and VSM techniques. The bands at 580−790 cm^{-1} and 3367 cm^{-1} corresponds to Fe−O vibrations and H-bonded OH groups. The diffraction planes at (2 2 0), (3 1 1), (4 0 0), (4 2 2), (5 1 1), and (4 4 0) correspond to face-cantered cubic Fe_3O_4. The average particle size of BMNPs and ACE−SMNPs were 10.39 nm and 2.38 nm, respectively. The presence of Fe and O in the nanoparticles were also confirmed from EDX spectra. The nanoparticles demonstrate high saturation magnetization, low remanent magnetization and coercivity, which facilitates easy magnetic separation and reuse. The dye removal efficiency of ACE−SMNPs is around 98.67% with a sequestration capacity of 38.64 mg g^{-1}. Pseudo-second-order kinetics and Langmuir isotherm best represented the equilibrium data. The dye removal process is endothermic, spontaneous, and governed by electrostatic and H-bonding interactions. The CBE-loaded nanoparticles were effectively regenerated and the renewed material shows removal efficiency nearly similar to fresh nanoparticles.

Department of Chemistry, National Institute of Technology Silchar, Silchar-788010, India

E-mail: md_a2002@rediffmail.com (M. Ahmaruzzaman); Tel.: +91-3842242915; Fax: +91-3842224797.

1. Introduction

Color is an integrated part of our life as the clothes we wear are of various colors, our foods are decorated with colors, and even our medicines are also colorful. And therefore, a lot of research have been undergoing in the production of color. This results in the global production of almost 10,000 different dyes and pigments, which amounts to more than 7×10^5 metric tons per year.[1] There are a variety of dyes such as acidic, basic, disperse, azo, and metal-complex dyes. However, azo dyes contribute nearly 70% to the total dye consumed in textile-processing and other industries, which marked them as the widely used class of dyes.[2] The incomplete fixation of dyes with target materials during the dyeing process results in the release of around 10-15% of dyes into the wastewater, which if not treated, causes environmental pollution.[3] Around 500 azo dyes based on carcinogenic amines are recognized as hazardous contaminants and benzidine (BZ; $(C_6H_4NH_2)_2$) based azo dyes are one of such pollutants.[4,5] Benzidine is known to be a human carcinogen based on sufficient evidences of carcinogenicity from studies in humans and animals. Oral exposure to benzidine caused mammary-gland cancer in female rats, liver cancer in mice and hamsters, and urinary-bladder cancer in dogs. Moreover, the reported studies have shown an association between benzidine exposure and cancer at other tissue sites such as liver, kidney, central nervous system, oral cavity, larynx, esophagus, bile duct, gallbladder, stomach, and pancreas.[6] Therefore, these dyes are declared as carcinogen and teratogen by the National Institute for Occupational Safety and Health (NIOSH), International Agency for Research on Cancer (IARC), and Environmental Protection Agency (EPA).[7] Nevertheless, these dyes are extensively used in textile dyeing processes. The dye-contaminated wastewater which could not be treated with conventional water purification techniques can be easily transported through sewers to natural water bodies. Especially, due to their synthetic origin, recycling nature, complex aromatic structure, toxic and carcinogenic degradation by-products; the treatment of these dye-

contaminated wastewater is a difficult task for researchers. Since, benzidine-based dyes are the inevitable source of environmental contamination; the removal of these dyes from wastewater is an important issue of the present era for environmental safety and protection.

Various technologies are available for the treatment of dye-contaminated wastewater such as, adsorption,[8,9] electrochemical adsorption,[10] biodegradation via free and immobilized cells,[11] photocatalytic degradation,[12] electrochemical oxidation,[13] and ion exchange.[14] Most physico-chemical methods are expensive and are greatly affected by other wastewater constituents, or generate waste products that need to be handled. Also, azo dyes are recalcitrant to conventional aerobic wastewater treatment processes and their persistence is mainly due to presence of sulfo and azo groups that do not occur naturally.[15] Adsorption is considered as one of the best treatment technology among all of these as it is a simple, fast, and efficient process which does not generate any hazardous by-products. Moreover, the spent adsorbents can be regenerated and reused. Therefore, in the present study adsorption technology was adopted for the removal of dyes from wastewater. The adsorption process is executed by means of natural or synthetic adsorbents. The use of natural adsorbents have been widely studied for dye removal and they are also associated with separation issues. Hence, the authors have considered magnetic nanoparticles for their promising use in wastewater treatment, which also nullify separation hazards.[16,17] The inevitable phenomenon of agglomeration associated with nanoparticles is also deal-with by the use of stabilizer in the synthesis of nanoparticles. Keeping in mind the growing need of greener materials, procedures, and technologies for environmental protection, the authors have exploited *Averrhoa carambola* extract (ACE) as a novel and green-stabilizer for the synthesis of stabilized nanoparticles. Herein, a simple chemical precipitation technique was employed for the synthesis of magnetite nanoparticles. The potential utilization of the fabricated nanoparticles have been explored for the removal of a carcinogenic and teratogenic BZ-based

azo dye−chlorazol black E from aquatic environment. The influence of operational parameters on the removal of dyes were studied, in addition to kinetics, isotherm, thermodynamics, and mechanism of dye removal. The regeneration and reusability of the exhausted nanoparticles were also explored to minimize waste generation and to justify its potential for long-term industrial applications.

2. Materials and methods

2.1 Chemicals and materials

The chemicals and reagents used in the present study were of analytical reagent grade and used as received, without any purification. The target compound−Chlorazol Black E (CBE; $C_{34}H_{25}N_9Na_2O_7S_2$, 781.73 g mol^{-1}) was procured from Sigma-Aldrich Chemical Co. Anhydrous $FeCl_3$ and $FeSO_4.7H_2O$ were supplied by Fisher Scientific (India). NaOH, HCl, and C_2H_5OH were obtained from Merck (India) Ltd. Ultrapure water (18.2 MΩ cm) used in the experiments was obtained from a Merck Millipore Direct-Q water purification system. The fruit−*Averrhoa carambola*, commonly known as star fruit, was brought from local markets.

2.2 Synthesis of novel stabilized magnetite nanoparticles

Herein, the authors have used a novel and green stabilizer−*Averrhoa carambola* extract (ACE) for the synthesis of stabilized magnetite nanoparticles. For the preparation of ACE, the fruit was cut into small pieces and squeezed mechanically to obtain the extract. The extract was centrifuged to remove bulk particles and the supernatant was used as the stabilizer. The nanoparticle synthesis was carried out by a simple chemical precipitation technique. In a typical synthesis route, 50 mL 0.5 M $FeSO_4.7H_20$ was mixed with 50 mL 0.75 M $FeCl_3$ solution. 25 mL 5 M NaOH was gradually added to the above mixture and continuously stirred at 343K for 30 min. The brown colour of the mixture slowly turned to black with the

formation of precipitate. Thereafter, 25 mL of the ACE was added and the resultant mixture was stirred for another 30 min, and aged for 6 h. The subsequent black precipitate was separated by a hand-held magnet and repeatedly washed with 50% ethanol-ultrapure water solution to remove impurities till pH of 7 was reached. The precipitate was vacuum-dried overnight in a vacuum desiccator, pulverized, sieved through a 150μ mesh, and stored in a desiccator till further use. The magnetic nanoparticles, thus obtained were labelled as *Averrhoa carambola* extract stabilized magnetite nanoparticles (ACE−SMNPs). For reference purpose, bare magnetite nanoparticles (BMNPs) were also synthesized as per the above procedure but, without the addition of the stabilizer.

2.3 Characterization tools and techniques

Fourier transform infra-red (FTIR) spectroscopic analysis of the samples were performed on a Nexus-870 (Thermo Nicolet, USA) FTIR Spectrometers, to study the surface functional groups of the nanoparticles. The KBr Pellet method was used for the preparation of samples for FTIR analysis, wherein 0.1 to 1.0 % sample was well-mixed with 200−250 mg of the dried KBr, and placed into a pellet-forming die to make the sample-pellets. When performing the measurements, the background correction was done to adjust for the infra-red light scattering losses in the pellet and for moisture adsorbed on the KBr. The crystallographic information of the synthesized nanomaterials were gathered from powder X-ray diffraction (P-XRD) studies performed on an X'Pert Pro XRD (PANalytical, Netherland) with Cu-K_α (λ = 0.154 nm) radiation at a voltage of 40 kV and tube current of 30 mA. The scanning range was from 10−70° and the scan rate was 2° min^{-1}. The selected area electron diffraction (SAED) patterns of the nanoparticles were recorded using a high resolution transmission electron microscope (HR-TEM; JEOL JEM-2100, Japan) with an acceleration voltage of 200 kV, LaB6 filament, and lattice resolution of 0.14 nm. The microstructure and composition analyses were also done with the aid of the HR-TEM equipped with energy dispersive X-ray

(EDX) analyzer (Oxford Instruments, U.K). The average particle size (from TEM images) and the lattice planes (from SAED patterns) of the nanoparticles were measured using Image J (1.48) software. In order to investigate the magnetic properties of the nanoparticles, vibrating sample magnetometer (VSM; Lakeshore 7410, U.S.A) was used. The magnetization parameters were measured at room temperature in an applied magnetic field of ±15 KOe. The initial and the residual CBE concentration were analysed using an UV-Visible Spectrophotometer (GENESYS 10S, Thermo Scientific, USA). The details of the procedure for analytical measurements and the mass-balance equations (S1 and S2) for the estimation of percentage removal and sequestration capacity of the nanoparticles are given in the Supporting information.

2.4 Removal of CBE in batch assay

In a typical batch operation, the removal of the target compound was performed in a series of 100 mL stoppered Erlenmeyer flasks. The effects of operational parameters such as, nanoparticle load (m), initial solution pH (pH_o), interaction time (t), initial dye concentration (C_o), and reaction temperature (T) were investigated. The experiments were conducted at 293K, 303K, and 313K, in a temperature-controlled incubator-cum-shaker (Alfa Instruments, India), at a shaking speed of 140 rpm. At the end of pre-determined time, the samples were withdrawn, centrifuged (Centrifuge, Remi Instruments, India) at 5000 rpm for 5 min, and the supernatant was analysed for residual dye concentration. The details of the procedures of batch assay are given in the Supporting information.

2.5 Regeneration of dye-loaded nanoparticles and their reusability studies

The regeneration of the dye-loaded nanoparticles were performed to minimize waste generation and reduce operating expenditure. A non-conventional regeneration technique was implemented, wherein, the exhausted nanoparticles were exposed to microwave (MW)

irradiation, and then interacted with a desorbing solvent. Herein, 0.1 M NaOH was used as a desorbing solvent because it shows promising results in regenerating anionic dye-loaded adsorbents.[9,18] Moreover, the solvent would not affect the surface property of the nanoparticles as they were synthesized using sodium hydroxide solution. In the regeneration process, the oven-dried CBE-loaded nanoparticles (at 383K for 1 h) were MW irradiated (2.45 GHz) at 360W for 5 min. Subsequently, the MW-treated materials were interacted with 20 mL 0.1 M NaOH for 30 min, and the regeneration efficiency was calculated with the help of Eq. (S3), given in the Supporting information. The effect of increasing MW irradiation, at 540W and 720W, on the regeneration of the exhausted nanoparticles were also studied. The regenerated nanoparticles were re-explored for three adsorption-regeneration cycles and the dye removal efficiencies, were calculated in each run.

2.6 Quality Assurance and Quality Control

To ensure the accuracy of the experimental data, all the measurement were made in triplicate, and the average values were reported. In parallel to test samples, blank experimental runs were also performed to establish accuracy, reliability, and reproducibility of the results. All the glasswares were pre-soaked overnight in 10% HNO_3 solution, rinsed with ultrapure water, and oven-dried, prior to their use in the experiments. The experimental data are graphically presented with error bars (5% of data) for more accurate representation of the experimental results.

3. Results and discussions

3.1 Characterization of magnetite nanoparticles

The surface functional groups of BMNPs and ACE−SMNPs are illustrated by the FTIR spectra shown in Fig. 1(a) and (b) respectively. The peaks observed at 580 cm^{-1} and 790 cm^{-1} for BMNPs and at 582 cm^{-1} and 790 cm^{-1} for ACE−SMNPs correspond to Fe–O vibrations,

which confirmed the formation of Fe_3O_4 nanoparticles. The spectra shows broad bands at around 3384 cm^{-1} and 3367 cm^{-1} for BMNPs and ACE−SMNPs, which may be assigned to H-bonded OH groups. These oxygen-containing functional groups are present on the surface of the nanoparticles.[19] Fig. 2(a) and (b) illustrates the XRD patterns of BMNPs and ACE−SMNPs respectively. The XRD patterns confirmed the face-centered cubic (fcc) structure of Fe_3O_4 in the nanoparticles (JCPDS card number 19-629). The diffraction peaks at 2θ values of 21.19°, 30.32°, 35.66°, 43.38°, 53.64°, 57.42°, and 62.97° were observed for BMNPs. Similar diffraction peaks at 21.06°, 30.25°, 35.73°, 43.28°, 53.61°, 57.35°, and 63.03° were shown by the XRD patterns of ACE−SMNPs. For both the nanoparticles, the detected peaks correspond to (1 1 1), (2 2 0), (3 1 1), (4 0 0), (4 2 2), (5 1 1), and (4 4 0) plane. The crystallite size of the nanoparticles were determined from the full width half maxima (FWHM) of the most intense diffraction peak (3 1 1) using Scherrer's equation (Eq. S4). The average crystallite size of the fabricated nanoparticles are calculated as 8.10 nm and 3.0 nm, for BMNPs and ACE−SMNPs respectively. The peak broadening of ACE−SMNPs as compared to BMNPs validates the narrow particle size of the stabilized nanoparticles.[20] The SAED patterns and the corresponding diffraction planes of BMNPs and ACE−SMNPs are displayed in Fig. 3(a) and (b). The concentric fused diffraction rings with some bright spots observed in the SAED patterns depict a polycrystalline nature of the nanoparticles. A lattice spacing of 0.295, 0.253, 0.209, 0.171, 0.161, and 0.148 nm, calculated from the SAED patterns of BMNPs and ACE−SMNPs correspond to (2 2 0), (3 1 1), (4 0 0), (4 2 2), (5 1 1), and (4 4 0) diffraction planes.[21] The results obtained, matches with that of the elucidation from XRD patterns.

The micro-structural information of the nanoparticles was gathered from the TEM images of BMNPs (Fig. 4(a)) and ACE−SMNPs (Fig. 4(b)). It is observed that BMNPs are mostly spherical in shape with some of the particles which grows into nano-rods. Furthermore,

agglomeration of nanoparticles is detected, which may be due to their low stability. However, in the case of ACE−SMNPs, the nanoparticles are stabilized at smaller particle size, which results in spherical nanoparticles with lower nanometers. The particle size diameter of BMNPs and ACE−SMNPs, as calculated from the TEM images range from 6.04–13.21 nm and 1.90–3.09 nm, respectively. The histograms in Fig. S1 and Fig. S2 depicts the particle size distribution from the TEM images of BMNPs and ACE−SMNPs, respectively. The average particle size of BMNPs is around 10.39 nm and that of ACE−SMNPs is 2.38 nm. The above findings of TEM investigations are nearly similar to XRD results. In this regard, it is worth mentioning that TEM is the first analytical tool to measure particle size and their distribution[22] whereas, XRD in accordance to Scherrer's equation, measure the average structural diameter of crystallite grains corresponding to the most intense diffraction peak.[23] The little difference in size (as predicted from TEM) indicates that the fabricated nanoparticles are not composed of similar crystallite grain sizes. The smaller crystallite grains may crystallize on the seeds of larger grains, which perhaps results in the increase of particle size as observed through TEM. Similar results were also reported in literature for the synthesis of iron oxide nanoparticles.[24] Fig. 5(a) and (b) represents the EDX spectra of BMNPs and ACE−SMNPs respectively. The presence of predominant peaks of iron (Fe) and oxygen (O) demonstrate the formation of the iron oxide nanoparticles. Table 1 shows the elemental composition of BMNPs and ACE−SMNPs. The major elemental composition of ACE is oxygen with minor composition of magnesium (Mg) and potassium (K). As this stabilizer was used in the synthesis of the ACE−SMNPs, an increase in the atomic weight% of O is observed (compared to BMNPs) in Fig. 5(b), with negligible content of Mg (0.09%) and K (0.06%). The room temperature magnetization curve of BMNPs and ACE−SMNPs are shown in Fig. 6(a) and (b). The magnetization parameters of BMNPs and ACE−SMNPs are shown in Table 2. It is evident from the Table that the ACE−SMNPs show lower values of

saturation magnetization (M_s=31.30 emu g^{-1}) than that of BMNPs (43.27 emu g^{-1}). This may be attributed to the presence of stabilizer and lower particle size of the ACE−SMNPs, which affects the magnetization parameters.[25] The observed low values of remanent magnetization (M_r) signifies good dispersability in solutions for reuse. The values of coercivity (H_c) almost equal to zero infers easy magnetic separation of the nanomaterials by an external magnet.[25] Therefore, the synthesized nanoparticles can be considered as potential magnetic nanomaterials in wastewater treatment for easy separation, recovery, and reuse.

3.2 Sequestration of CBE and the influence of operational parameters

The removal of CBE was explored in a batch operation to study the effect of operational parameters such as, nanoparticle load, solution pH, interaction time, reaction temperature, and initial dye concentration on the dye removal efficiency. To study the influence of nanoparticle load (m) on the removal efficiency of CBE, experiments were performed by the interaction of 20 mL CBE solution (100 mg L^{-1}) with nanoparticles in the load range of 0.25−6 g L^{-1}. The observed results were depicted in Fig. 7(a), which demonstrates that with a nanoparticle load of 5 g L^{-1}, BMNPs shows CBE removal of 32.83% whereas, 98.67% removal was achieved by ACE−SMNPs. Thus, ACE−SMNPs is a better sorbent as compared to BMNPs for the removal of CBE and hence, further studies were carried out with ACE−SMNPs. The uptake of CBE onto ACE−SMNPs significantly increases with the increase in m up to 5 g L^{-1} and thereafter reached a plateau line. A marginal percent removal of 0.38% was observed at m in the range of 5−6 g L^{-1}. Thus, the nanoparticle load of 5 g L^{-1} was considered as the optimum load for further studies. The observed uptake profile of CBE onto ACE−SMNPs can be ascribed to the fact that there exists a concentration gradient between the nanoparticle surface and the bulk of the dye solution. At lower m, a high concentration gradient occurs, which increases the competing tendency of the CBE molecules to get adhered to the accessible surface functional groups of ACE−SMNPs. The dye removal efficiency increase at the initial

stage due to the availability of larger surface area, more adsorption sites, and active surface functional groups.[26] But, a marginal rise in removal efficiency was observed at later stage, which is due to the attainment of adsorption equilibrium.

The change in solution pH (pH_o) affects the zeta potential on the surface of the ACE−SMNPs, which consequently affects the dye removal process. The point of zero charge (pH_{ZPC}) of magnetite nanoparticles is around 6.4 and at pH_{ZPC}, the surface of the nanoparticles is neutral. Fig. 7(b) demonstrates the effect of solution pH on the removal of CBE. It is observed that the percent removal of CBE drastically decreases after pH 6. A percent removal of 24.57% was achieved at pH 10 whereas, at pH range of 2−6, maximum percent removal (99.57−98.67%) of CBE was observed. It can be explained from the concept of zeta potential that at pH<pH_{ZPC}, the surface of the ACE−SMNPs is positively charged whereas, the dye is negatively charged (CBE is an anionic dye). Thus, an electrostatic force interaction comes into play between the dye molecules and the nanoparticles, which results in the higher uptake of CBE onto ACE−SMNPs. However, at pH>pH_{ZPC}, both the dye molecules and the nanoparticle surface are negatively charged and electrostatic repulsion is anticipated, which results in the decrease of dye removal efficiency.

Fig. 7(c) shows that the percent removal of the dye increases with increasing interaction time. A percent removal of 6.64% is observed at initial 15 min, which gradually increases to 27.71% at the end of 1 h and to 98.15% at 8 h. This is followed by marginal increase in percent removal (1.4%) till 24 h, designated by a plateau line. The residual CBE concentration in the solution was 1.85% after 8 h, 0.95% after 12h, and 0.45% after 24 h of interaction time. The negligible difference in residual CBE concentration demonstrates the attainment of a steady state quasi-equilibrium at 8 h.

The impact of initial CBE concentration ($50 \leq C_o \leq 400$ mg L^{-1}) on the percent removal and sequestration capacity of ACE−SMNPs is illustrated in Fig **7**(d). An increase in sequestration capacity of the nanoparticles is observed with the increase in initial CBE concentration. This observation can be explained from the anticipation of greater mass driving force with higher dye concentration, which results in the enhancement of CBE uptake. Contrary to the above, with increasing dye concentration, the dye molecules compete with one another to get adhered to the limited active sites on the nanoparticle surface and consequently, percent removal of CBE decreases.[26] The percent removal of CBE increases with the increasing reaction temperature, as shown in Fig. **7**(e). This confirms the endothermic nature of the dye removal process. The percent removal increased from 95.75−99.55% as the reaction temperature increases from 293−313K. The above observation can be attributed to the attainment of adequate energy by the dye molecules, which increases its mobility to enter the active sites of the nanoparticles.

3.3 Kinetics, isotherm, and thermodynamics of dye removal

The kinetic investigation on the dye removal process helps to understand the equilibrium time and the mass transfer of the dye molecules. The equilibrium data at different time intervals were examined by kinetic models such as, pseudo-first-order, pseudo-second-order, Webber-Morris intraparticle diffusion, and kinetics of mass transfer. The mathematical expressions of the kinetic models (S5–S8) and their corresponding normalized standard deviation (Δq %) (S9) are given in the Supporting information. The kinetics of CBE removal was studied and the various kinetic parameters (Table 3) were obtained from linear regression of kinetic models such as, pseudo-first-order, pseudo-second-order, intraparticle diffusion, and kinetics of mass transfer (Fig. 8(a-d)). Pseudo-second-order kinetic model best fit the equilibrium data with better correlation co-efficient (R^2=0.999) and least normalized standard deviation ($\Delta q\%$=0.039). Moreover the calculated q_e value is closer to the experimental q_e value. The

boundary layer effect, as observed from the C values of first, second, and third step of Fig. 8(c) corresponds to boundary layer, mesoporous, and microporous diffusion, respectively. The value of transport number (n) as calculated from Eq. (S8) indicates the type of transport mechanism. $n \leq 0.5$ signify Fickian mechanism and $n \geq 1$ represents non-Fickian transport.[27] The value of n (0.174) and k (0.676) are calculated from the curve (Fig. 8(d)), which fits the non-linear mass transfer data with R^2=0.956. Thus, the curve represents that Fickian transport mechanism controls the diffusion of the CBE molecules into the pores of the nanoparticles during the sequestration process.

The investigation of adsorption isotherm on the removal of CBE was performed by fitting the data to some isotherm models (S10−S11), which is a vital step to characterize the removal phenomena. Fig. 9 shows the linearized data fitting for Langmuir and Freundlich isotherms, in addition to the experimental isotherm and its validity plot at 303K. Table 4 illustrates the isotherm parameters for CBE removal by the ACE−SMNPs. A linear relationship between C_e/q_e vs C_e (Fig. 9(a)) demonstrates the validity of Langmuir isotherm (R^2=0.985). The monolayer coverage of CBE molecules onto the nanoparticles provides a sequestration capacity of 38.64 mg g^{-1}. The feasibility of the Langmuir isotherm is ascertained with dimensionless separation factor (R_L) (Eq. S12).The removal process is favourable when $0<R_L<1$, unfavourable ($R_L>1$), linear ($R_L=1$), and irreversible ($R_L=0$). In the present study, as the value of R_L is less than 1, the removal of CBE is favourable in nature.[28] The assessment of Freundlich isotherm (Fig. 9(b)) parameters show substantial K_F values with $1/n$ <1, which indicates favourable removal of CBE. However, the Freundlich isotherm is characterized by lower R^2 value (0.88) as compared to that of Langmuir isotherm. The error analysis of the fit to the isotherm equations are performed with the help of Marquardt's percent standard deviation (MPSD) error function (Eq. S13). On the basis of correlation co-efficient (R^2) closest to unity and minimal errors for the two isotherms at 303K, the fitting is

Freundlich<Langmuir. The experimental isotherm and its validity with other standard isotherms is represented in Fig. 9(c). It is observed that Langmuir isotherm profile is closer to the experimental data with lesser deviation than the Freundlich isotherm.

The thermodynamic parameters of CBE removal were evaluated from the thermodynamic equations (S14−S16) given in the Supporting information. The slope and intercept of van't Hoff plot (*ln* K_{ad} versus *1/T*; Fig. 10(a)) gives the enthalpy (ΔH) and entropy (ΔS) of the dye removal system. The estimated thermodynamic parameters are listed in Table 5. The data shows that the value of ΔH is positive, which signifies the existence of an energy barrier in the dye removal process and thus, confirm the endothermic nature of sequestration. The positive value of ΔS is an indication of the randomness of the system at solid/liquid interface. During the process, CBE dislodge the adsorbed water molecules from the nanoparticle surface thereby gaining more translational entropy than lost by the CBE molecules due to adsorption. Consequently, the randomness of the system increases. Similar results were reported in literature for the adsorption of tannery dye.[29] The decrease in ΔG values with the rise in temperature implies the spontaneity and feasibility of the sequestration phenomena.

3.4 Mechanism of CBE removal

Electrostatic interactions between the dye molecules and nanoparticle surface administer the sequestration of CBE from aqueous solutions. The electrostatic interactions of CBE and ACE−SMNPs with changing solution pH is discussed in detail in *Sec. 3.2*. It is evident from the discussion that the electronegative $-SO_3H$ group of CBE is electrostatically attracted to the positive surface of ACE−SMNPs, at pH<pH_{ZPC} and hence, an increased dye removal efficiency was achieved at a pH range of 2−6. Furthermore, the mechanism of dye removal was also investigated from the FTIR spectra (Fig. 10(b)) of the CBE-loaded ACE−SMNPs. The FTIR peak at 3367 cm^{-1} observed for ACE−SMNPs corresponds to the functional group –

OH. The H-atom of the hydroxyl group can form H-bonding with the functional groups such as, $=O^-$ and $-SO3^-$ of the chlorazol black E molecules in solution. As a result of the formation of H-bonding, the stretching vibration of the band decreases from 3367 cm^{-1} to 3359 cm^{-1} with peak broadening. Similar shifting of hydroxyl bands to lower vibrational frequencies due to the formation of H-bonding have been observed for graphene oxide loaded dopamine.[30] Thus, H-bonding takes part in the dye removal process. The absorption bands at 582 cm^{-1} shifted to 570 cm^{-1} post adsorption of CBE onto the nanoparticles. Moreover, some of the absorption bands are unaffected after the sequestration process, which confirms that they do not take part in the sequestration phenomena. However, the exact mechanism of sequestration is a complex phenomenon and need to be explored in detail for better understanding of the process.

3.5 Regeneration and reusability

The exhausted CBE-loaded ACE−SMNPs were regenerated by a non-conventional regeneration technique as discussed in *Sec. 2.5*. The regeneration efficiency of the dye-loaded nanoparticle was 99.25%. Due to the MW irradiation of the exhausted nanoparticles, the adsorbed CBE molecules move toward the material surface and subsequently, the desorbing solvent can easily remove them. In the case of conventional heating by convection, the gases at high temperature transport from the surface to the centre of the irradiated material. However, in MW heating, the irradiated material is heated from the inner core, which develops a decreasing temperature gradient towards the surface.[31] Hence, an easy transport of the desorbed molecules from higher temperature core region to lower temperature surface takes place. Thus, the textural characteristics of the material are conserved by reducing coke deposits in the porous domain. Contrary to the above, convection heating decomposes the desorbed molecules and rupture the pore walls, which eventual results in the loss of textural properties of the material.[32]

The regenerated ACE−SMNPs were reused for the removal of CBE. The renewed material shows 98.36, 97.82, and 97.15% dye removal efficiency at first, second, and third cycle, respectively. The dye removal efficiency decreased to 94.67% and 90.24%, when MW irradiation increased to 540W and 720W respectively. This observation may be due to the partial decomposition of the dye molecules at higher irradiation, which results into coke deposits and pore blockages. Besides, there may occur a drop in the oxygen-containing surface functional groups at higher temperature.[32]

4. Conclusion

Herein, it is established that *Averrhoa carambola* extract is effective as a stabilizer in the synthesis of stabilized magnetite nanoparticles. The present attempt is a green synthesis route, which is an advancement in the utilization of natural products for the development of technological materials for sustainable environmental applications. ACE−SMNPs shows promising and high uptake of the dye (98.67 %) as compared to BMNPs (32.83%) for nanoparticle load of 5 g L^{-1} and at an equilibrium interaction time of 8 h. The nanoparticles possess sequestration capacity of 38.64 mg g^{-1}. The dye removal process follows pseudo-second-order kinetics and Langmuir isotherm, with higher R^2 values and minimal deviation. The evaluation of thermodynamic parameters confirm the endothermic and spontaneous nature of adsorption. Electrostatic and H-bonding interactions administer the removal of CBE. The exhausted nanoparticles were effectively regenerated (99.25%) with MW irradiation followed by interaction with 0.1 M NaOH. The renewed material shows dye removal efficiency of 98.36, 97.82, and 97.15% at first, second, and third adsorption-regeneration cycle. Hence, ACE−SMNPs can be considered as a potential magnetic nanomaterial for the removal of chlorazol black E from aqueous solution.

Acknowledgements

Md. Juned K. Ahmed gratefully acknowledges the Ministry of Minority Affairs (MoMA), Government of India and University Grant Commission (UGC), New Delhi for financial assistance under the Maulana Azad National Senior Research Fellowship (MANSRF). Authors are thankful to the National Institute of Technology Silchar for providing laboratory facilities.

References

1. Y. S. Al-Degs, M.I. El-Barghouthi, A. H. El-Sheikh, G. M. Walker, *Dyes Pigments*, 2008, **77,** 16–23.
2. S. T. Ambrosio, G. M. Campos-Takaki, *Bioresour. Technol*., 2004, **91,** 69−75.
3. N. Fernandes, C. A. Almeida, N. A. Debacher, M. M. Souza Sierra, *J. Mol. Str*., 2010, **982,** 62–65.
4. K. Golka, S. Kopps, Z. W. Myslak, *Toxicol. Lett*., 2004, **151,** 203–210.
5. M. Ghaedi, H. Hossainian, M. Montazerozohori, A. Shokrollahi, F. Shojaipour, M. Soylak, M. K. Purkait, *Desalination*, 2011, **281,** 226–233.
6. B. W. Manning, C. E. Cerniglia, T. W. Federle, *Appl. Environ. Microbio.,* 1985, **50,** 10−15.
7. M. Ghaedi, A. Najibi, H. Hossainian, A. Shokrollahi and M. Soylak, *Toxicol. Environ. Chem.,* 2012, **94,** 40−48.
8. S. K. Rhee, G. M. Lee, S. T. Lee, *Appl. Microbiol. Biotechnol*., 1996, **44,** 816–822.
9. M. Ahmaruzaman, Md. J. K. Ahmed, S. Begum, *Desal. Water Treat*., 2014, DOI: 10.1080/19443994.2014.950995.
10. Q. Lin, W. Dhongui, W. Jianlong, *Bioresour. Technol*., 2010, **101,** 5229–5234.
11. H. Zhao, S. Xu, J. Zhong, X. Bao, *Catal. Today*, 2004, **857,** 93–95.

12. V. K. Gupta, R. Jain, A. Mittal, T. A. Saleh, A. Nayak, S. Agarwal, S. Sikarwar, *Mater. Sci. Eng. C Mater. Bio. Appl*., 2012, **32,** 12−17.

13. N. Q. Zhao, T. C. Zhou, C. S. Shi, J. J. Li, W. K. Guo, *Mater. Sci. Eng. B*, 2006, **127,** 207–211.

14. D. Suteu, D. Bilba, S. Coseri, *J. Appl. Polymer Sci*., 2014, DOI: 10.1002/app.39620.

15. W. Bi, R. B. Hayes, P. Feng, Y. Qi, X. You, J. Zhen, et al., *Am. J. Ind. Med*., 1992, **21,** 481−489.

16. Md. J. K. Ahmed, M. Ahmaruzzaman, *Water Sci. Technol*., 2015, **71,** 1361−1366.

17. N. M. Mahmoodi, *J. Ind. Eng. Chem*., 2015, **27,** 251−259.

18. A. Mittal, J. Mittal, A. Malviya, V. K. Gupta, *J. Colloid Interface Sci*. 2009, **340,** 16−26.

19. L. Ai, C. Zhang, F. Liao, Y. Wang, M. Li, L. Meng, J. Jiang, *J. Hazard. Mater*., 2011, **198,** 282–290.

20. N. Yang, S. Zhu, D. Zhang, S. Xu, *Mater. Lett*., 2008, **62,** 645–647.

21. R. Xiong, Y. Wang, X. Zhang, C. Lu, *RSC Adv.,* 2014, **4,** 22632−22641.

22. G. H. Woehrle, J. E. Hutchison, S. Ozkar, R. G. Finke, *Turkish J. Chem.,* 2006, **30,** 1−13.

23. C. Hammond. The Basics of Crystallography and Diffraction, *Oxford University Press,* New York, USA, 1997.

24. Y-K. Sun, M. Ma, Y. Zhang and N. Gu, *Colloids Surfaces A,* 2004, **245,** 15−19.

25. E. Darezereshki, F. Bakhtiari, A. B. Vakylabad, Z. Hassani, *Mater. Sci. Semicond. Proc*., 2013, **16,** 221–225.

26. Md. J. K. Ahmed, M. Ahmaruzzaman, R. A. Reza, *J. Colloid Interface Sci*., 2014, **428,** 222−234.

27. M. Ahmaruzzaman, S. L. Gayatri, *J. Chem. Eng. Data*, 2010, **55,** 4614−4623.

28. K. Srinivasan, N. Balasubramanian, T. V. Ramakrishna, *Indian J. Environ. Health*, 1988, **30,** 376−387.

29. R. Baccar, P. Blanquez, J. Bouzid, M. Feki, H. Attiya, M. Sarra, *Fuel Proc. Technol*., 2013, **106,** 408–415.

30. H. Ren, D. D. Kulkarni, R. Kodiyath, W. Xu, I. Choi, V. V. Tsukruk. *ACS Appl. Mater Interfaces*, 2014, **6,** 2459−2470.

31. P. Liao, S. Yuan, W. Xie, W. Zhang, M. Tong, K. Wang, *J. Colloid Interface Sci*., 2013, **390,** 189–195.

32. C. O. Ania, J. B. Parra, J. A. Menendez, J. J. Pis, *Micropor. Mesopor. Mater*., 2005, **85,** 7–15.

Table 1 Elemental composition of the nanoparticles from EDX.

Nanoparticles	Element	Weight%	Atomic%
BMNPs	O K	36.94	67.16
	Fe K	63.06	32.84
	Total	100	
ACE−SMNPs	O K	39.1	69.1
	Mg K	0.07	0.09
	K K	0.08	0.06
	Fe K	60.75	30.76
	Total	100	

Table 2 Magnetization parameters of the synthesized nanoparticles.

Parameters and units	BMNPs	ACE−SMNPs
M_s (emu g^{-1})	43.27	31.3
M_r (emu g^{-1})	1.37	1.42
H_c (KOe)	0.0235	0.0255
Squareness (M_r/M_s)	0.031	0.045

Table 3 Kinetic parameters for the removal of CBE by ACE−SMNPs.

Model	Parameters	Units	Values		
Pseudo-first-order	$q_{e,\,exp}$	mg g^{-1}	19.63		
	$q_{e,\,cal}$	mg g^{-1}	21.64		
	k_1	h^{-1}	0.409		
	R^2		0.991		
	Δq	%	3.87		
Pseudo-second-order	$q_{e,\,cal}$	mg g^{-1}	19.98		
	k_2	g mg^{-1} h^{-1}	0.015		
	R^2		0.996		
	Δq	%	0.728		
			first step	*second step*	*third step*
Intraparticle diffusion	k_{ip}	mg $g^{-1}h^{1/2}$	9.32	4.73	0.12
	C	mg g^{-1}	3.63	6.26	19.32
	R^2		0.986	0.999	0.721

Table 4 Isotherm parameters for the sequestration of CBE onto ACE−SMNPs.

Langmuir isotherm					
Temp. (K)	**a_L (mg g^{-1})**	**b_L (L mg^{-1})**	**R_L**	**R^2**	**MPSD**
303	38.64	0.171	0.055	0.985	1.17
Freundlich isotherm					
Temp. (K)	**$1/n_F$**	**K_F (L mg^{-1})**		**R^2**	**MPSD**
303	0.174	14.72		0.88	4.56

Table 5 Thermodynamic parameters of CBE removal by ACE−SMNPs.

Temp. (K)	ΔG (kJ mol^{-1})	ΔH (kJ mol^{-1})	ΔS (kJ $K^{-1}mol^{-1}$)	R^2
293	− 7.23			
303	− 10.72	94.96	0.349	0.999
313	− 14.20			

Figure Captions:

Fig. 1 FTIR spectra of (a) BMNPs and (b) ACE−SMNPs.

Fig. 2 XRD patterns of (a) BMNPs and (b) ACE−SMNPs.

Fig. 3 SAED patterns of (a) BMNPs and (b) ACE−SMNPs.

Fig. 4 TEM images of (a) BMNPs and (b) ACE−SMNPs at 100, 50, and 2 nm.

Fig. 5 EDX spectra of (a) BMNPs and (b) ACE−SMNPs.

Fig. 6 Room-temperature magnetization curves of (a) BMNPs and (b) ACE−SMNPs.

Fig. 7 Influence of operational parameters on the removal of CBE, (a) nanoparticle load (m); C_o=100 mg L^{-1}, t=8 h, T=303K, (b) intial solution pH (pH_o); C_o=100 mg L^{-1}, m=5 g L^{-1}, t=8 h, T=303K, (c) interaction time (t); C_o=100 mg L^{-1}, m=5 g L^{-1}, T=303K, (d) initial concentration (C_o); m=5 g L^{-1}, t=8 h, and (e) reaction temperature (T); C_o=100 mg L^{-1}, m=5 g L^{-1}, t=8 h.

Fig. 8 (a) Pseudo-first-order kinetics, (b) pseudo-second-order kinetics, (c) intraparticle diffusion, and (d) non-linear kinetics of mass transfer for the removal of CBE by ACE−SMNPs; C_o=100 mg L^{-1}, T=303K, m=5 g L^{-1}.

Fig. 9 (a) Langmuir isotherm, (b) Freundlich isotherm, and (c) validity of different isotherms with respect to the experimental isotherm for the removal of CBE by ACE−SMNPs at 303K.

Fig. 10 (a) van't Hoff plot and (b) interaction of CBE with ACE−SMNPs as predicted from FTIR spectroscopy.

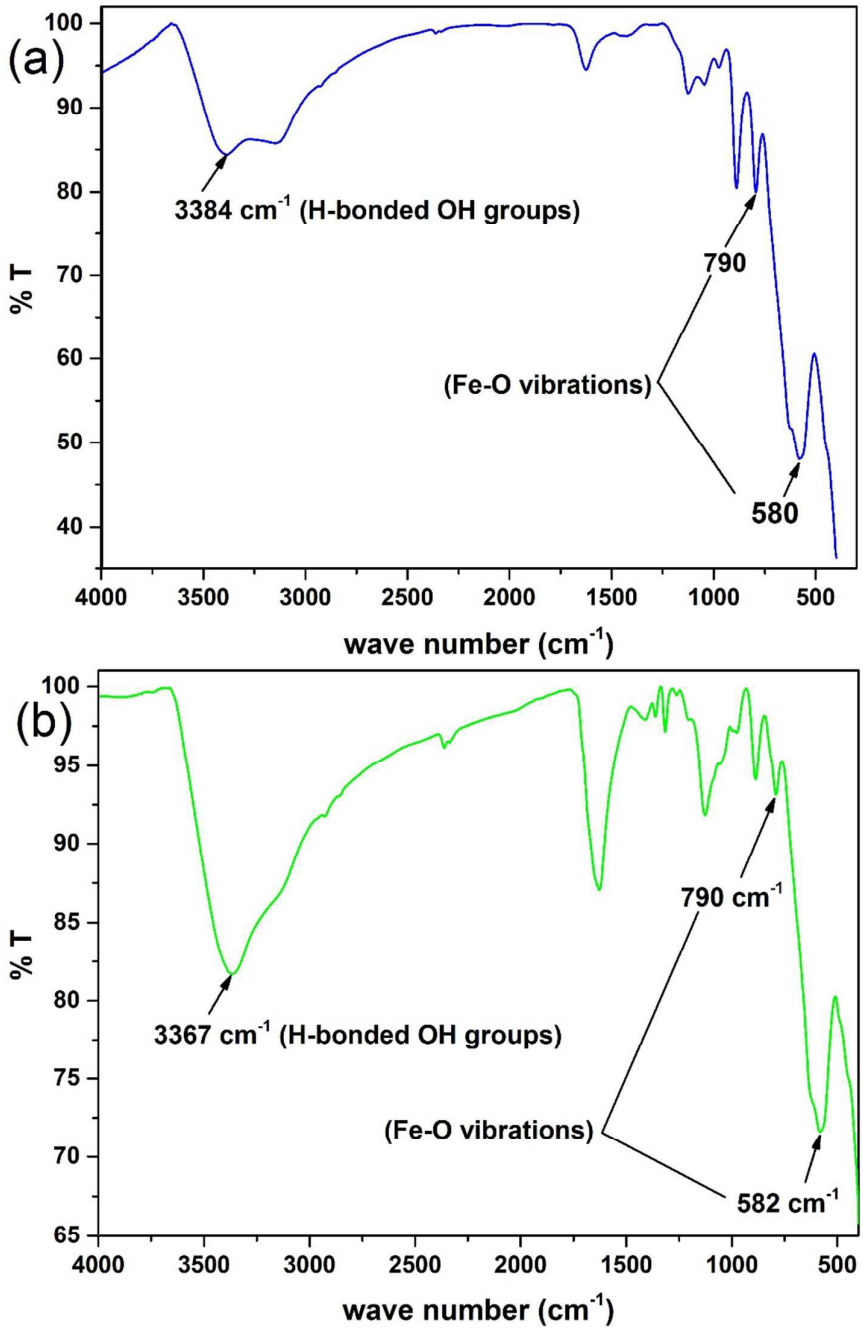

Fig. 1

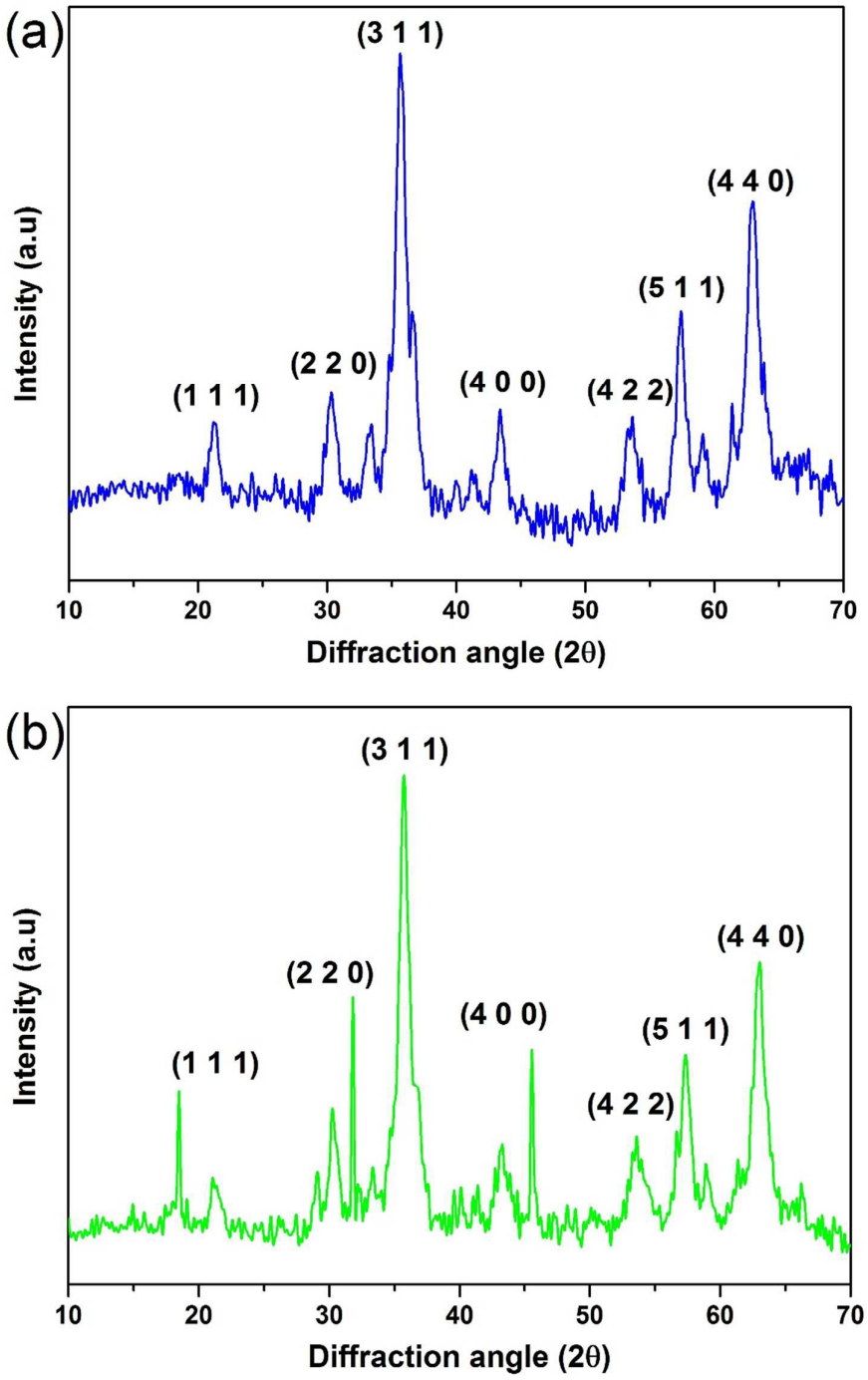

Fig. 2

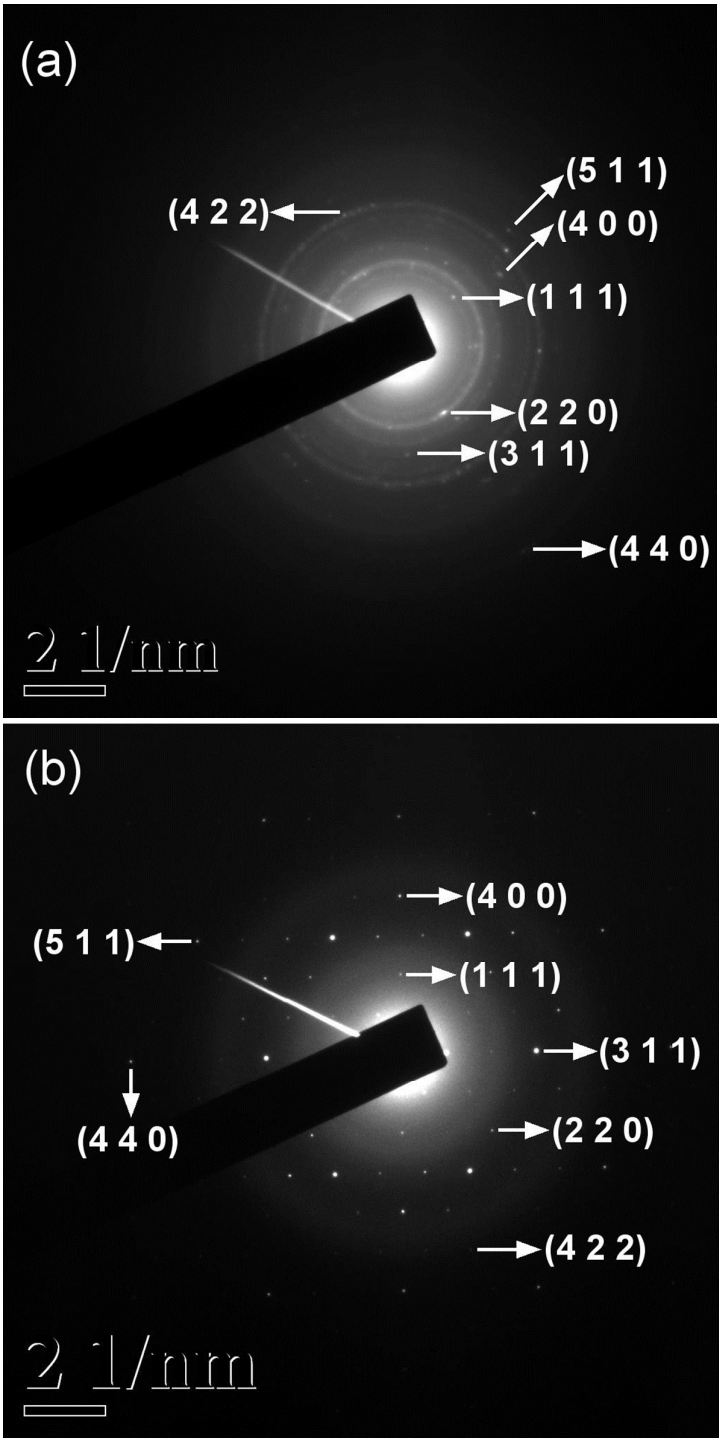

Fig. 3

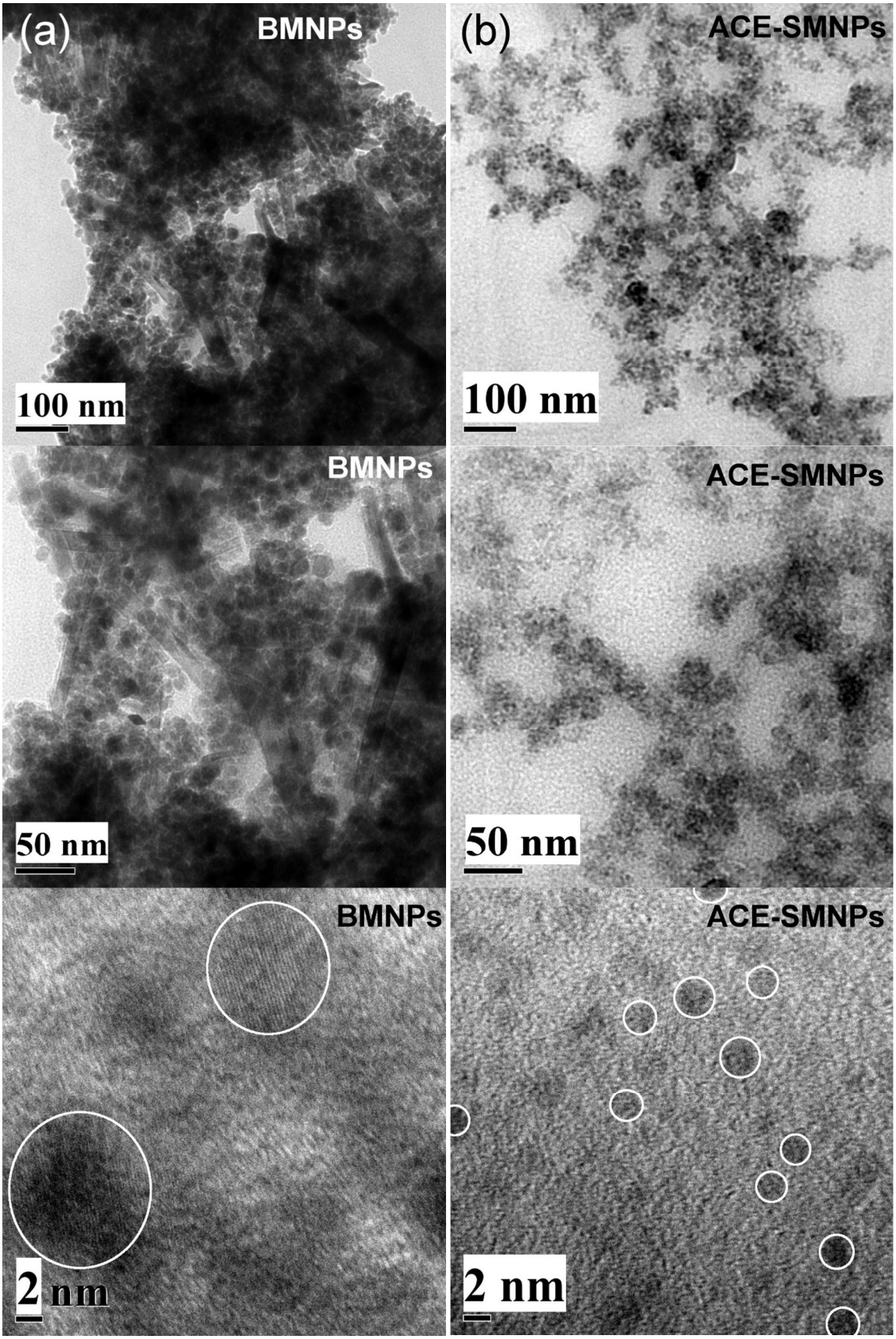

Fig. 4

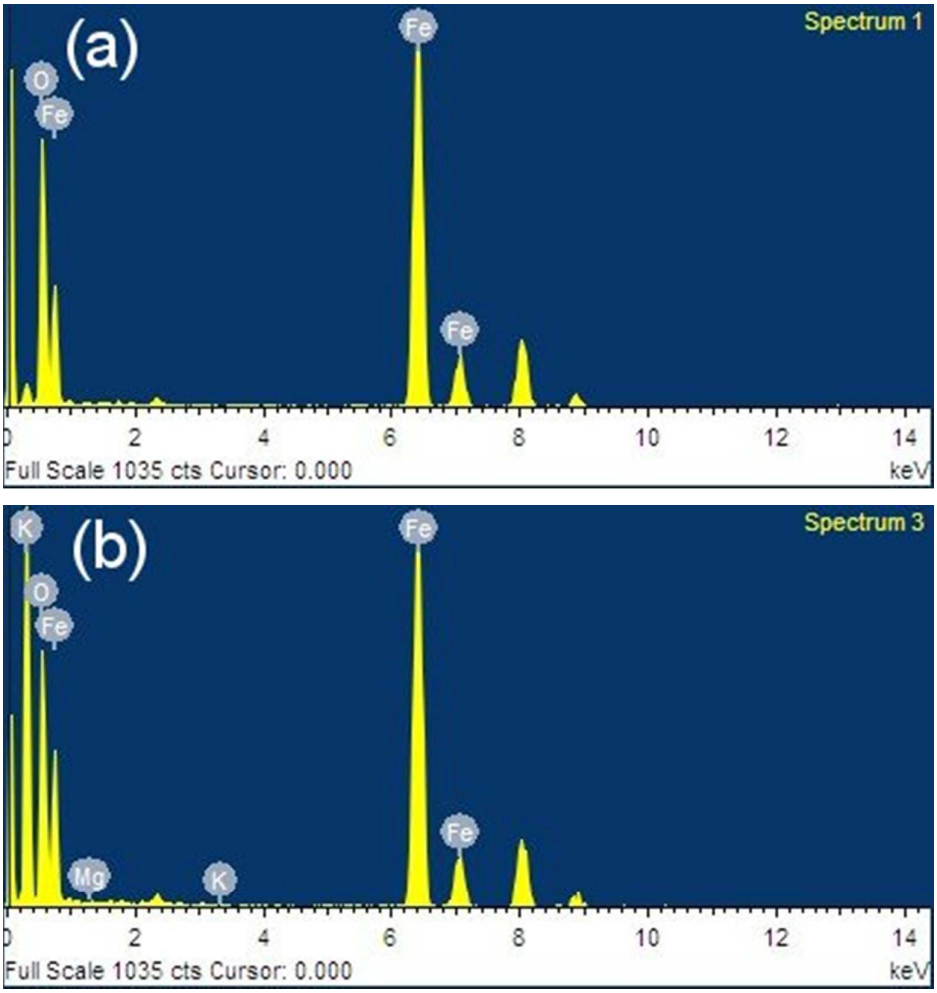

Fig. 5

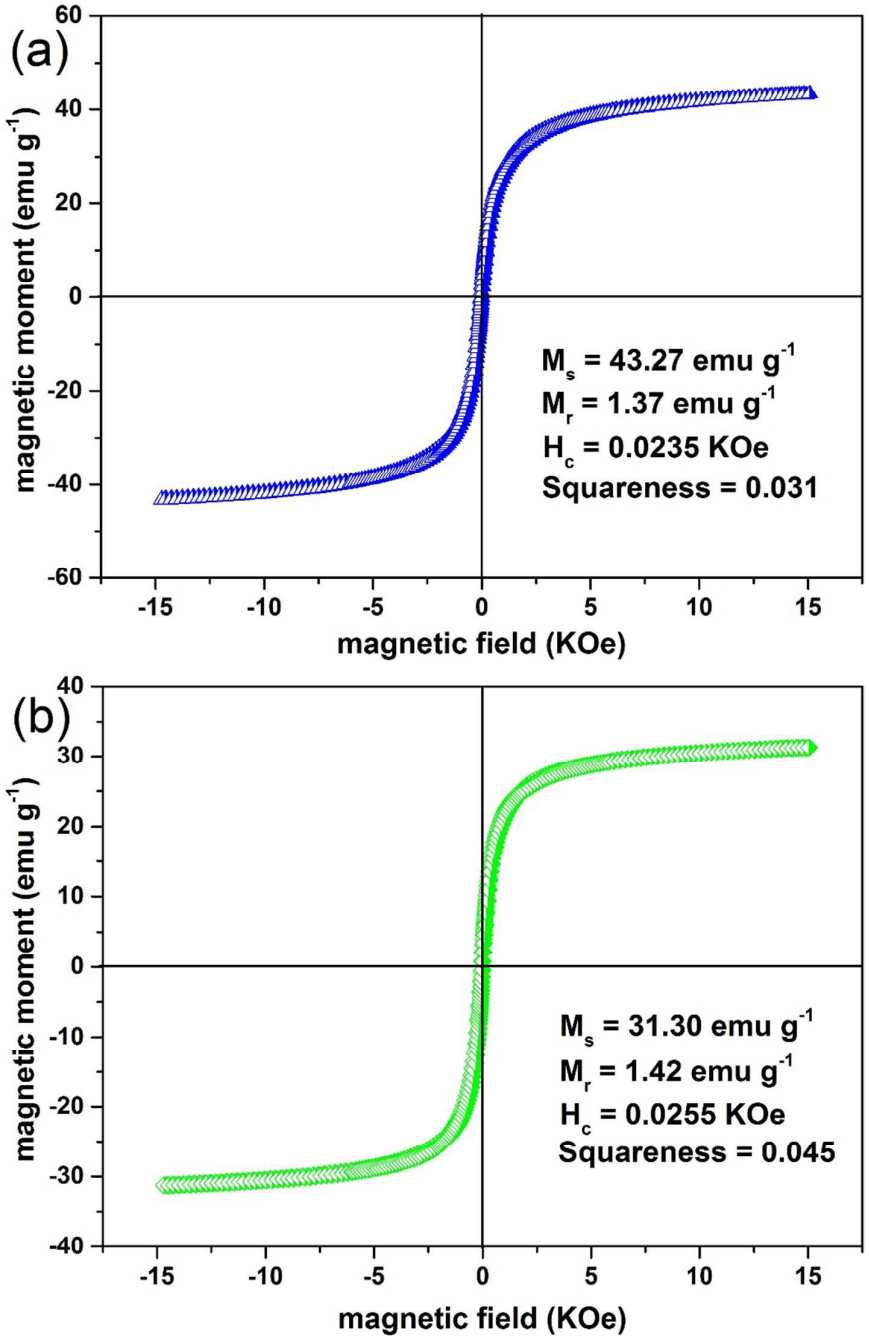

Fig. 6

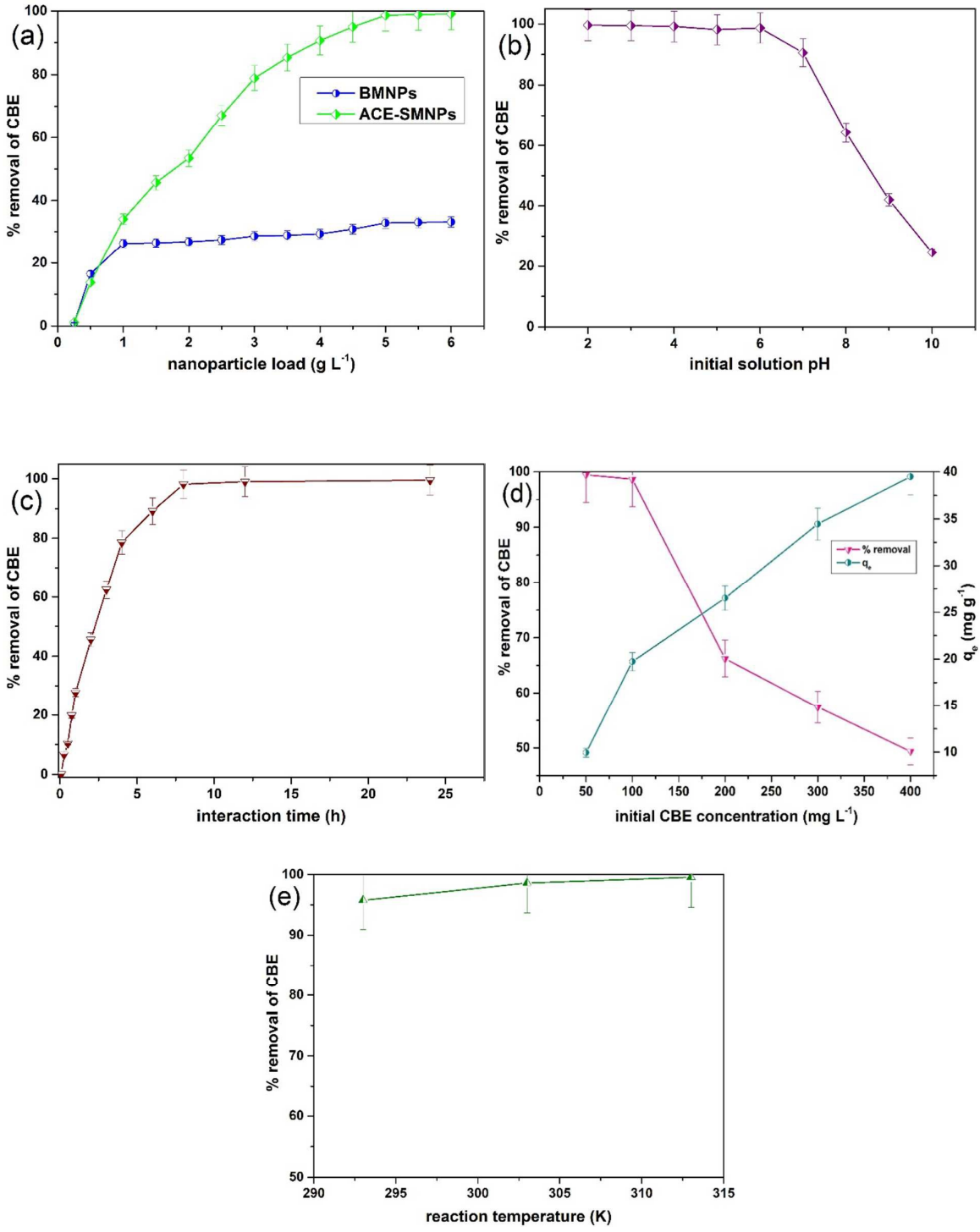

Fig. 7

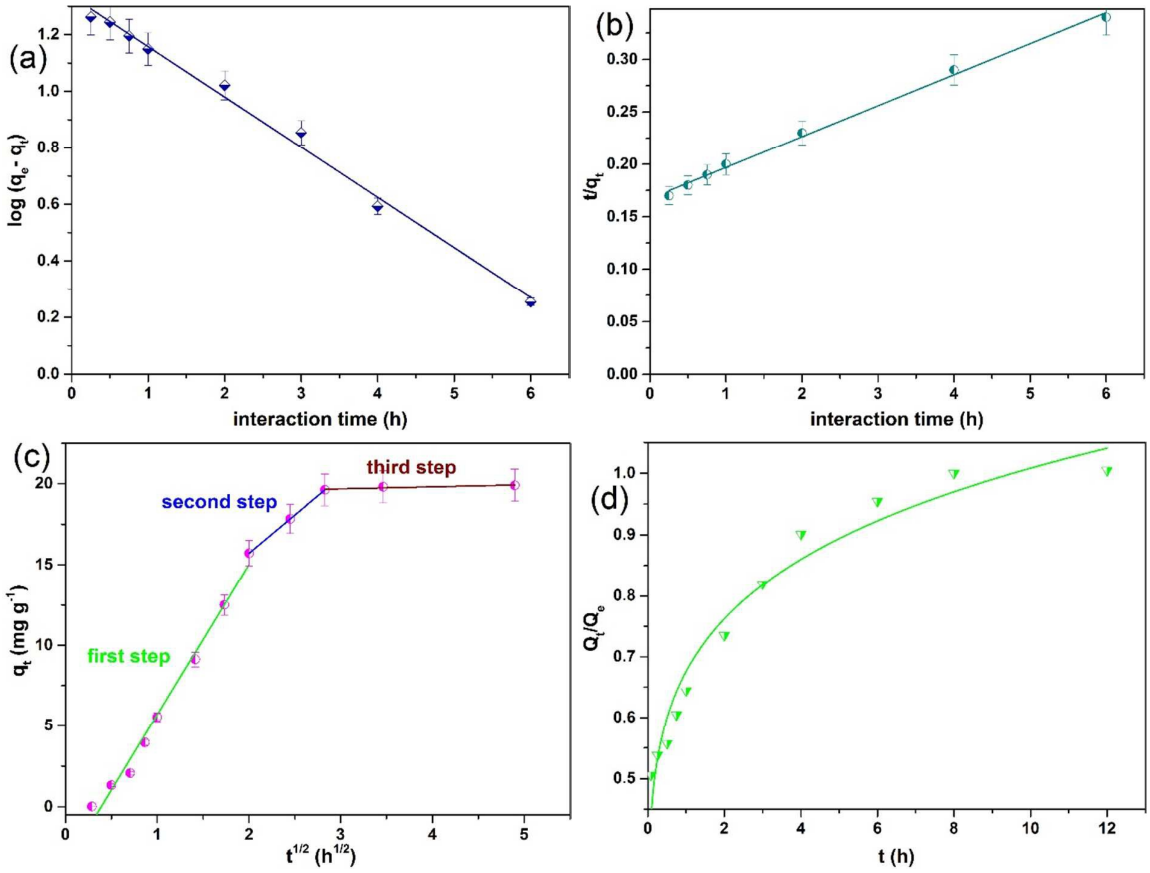

Fig. 8

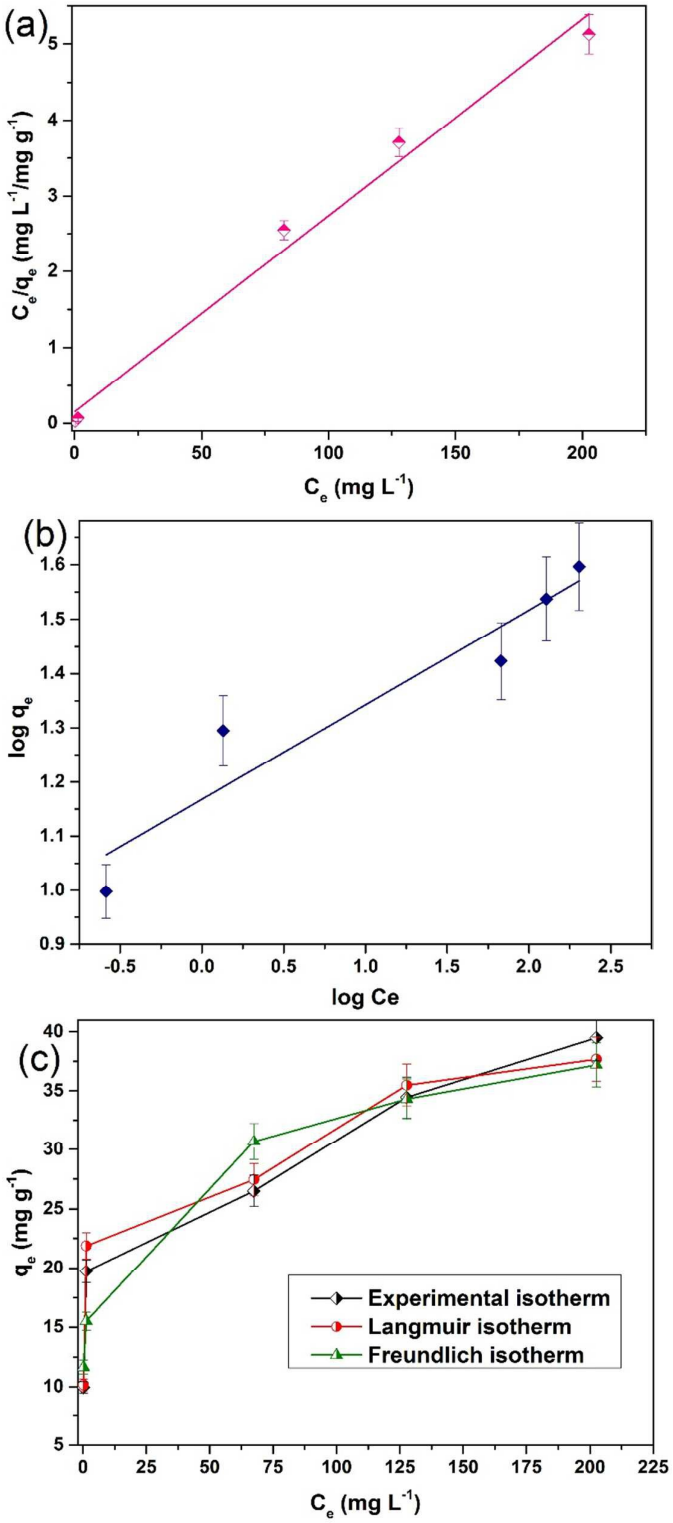

Fig. 9

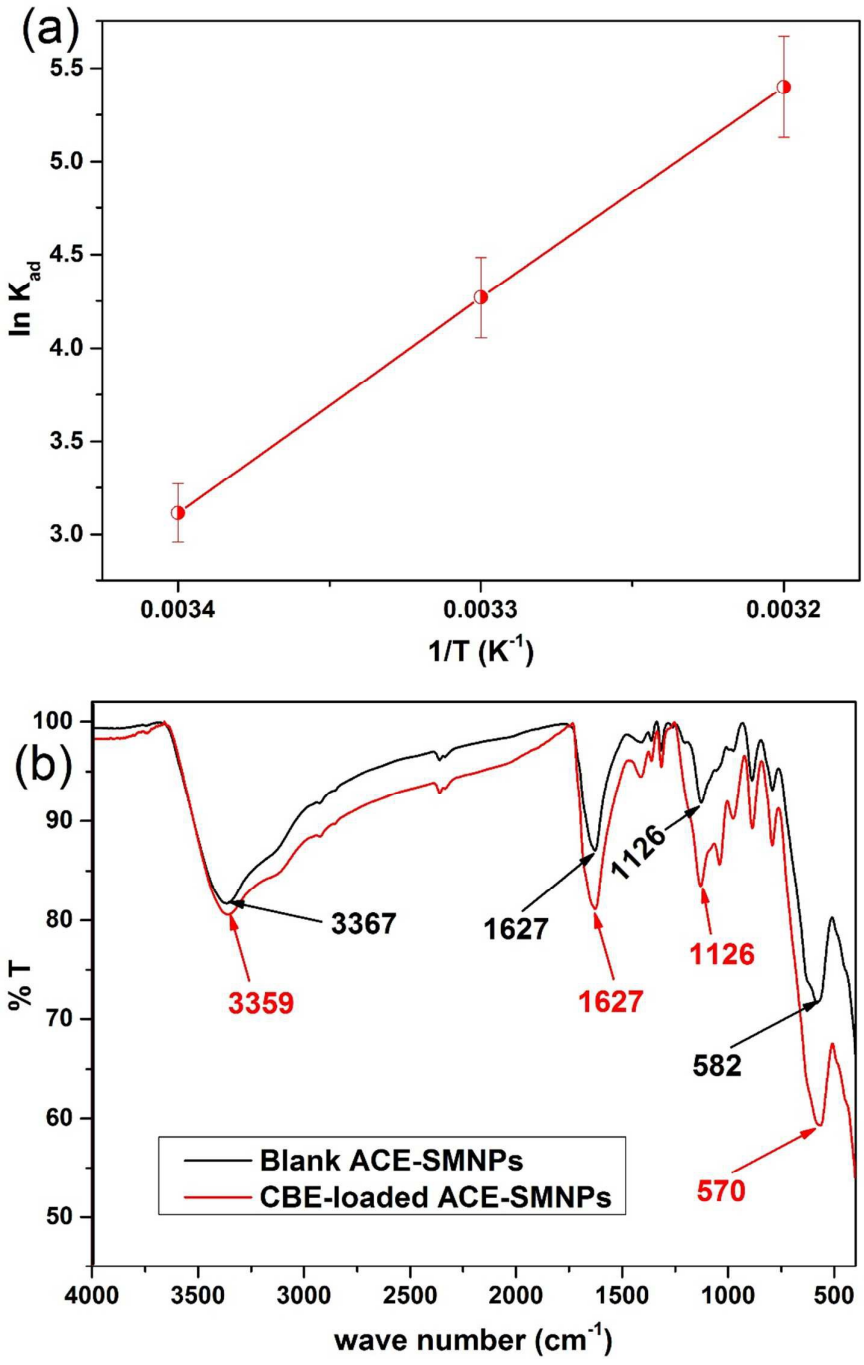

Fig. 10